ADVANCED MATERIALS

Supporting Information

Robust Artificial Interphases Constructed by a Versatile Protein-Based Binder for High-Voltage Na-Ion Battery Cathodes

Huangxu Li, Chaohong Guan, Jie Zhang, Ke Cheng, Qingxin Chen, Liang He, Xiaochen Ge, Yanqing Lai,* Hongyan Sun,* and Zhian Zhang*

Supplementary material

Robust Artificial Interphases Constructed by a Versatile Protein-Based Binder for High-Voltage Na-Ion Battery Cathodes

Huangxu Li, Chaohong Guan, Jie Zhang, Ke Cheng, Qingxin Chen, Liang He, Xiaochen Ge, Yanqing Lai,* Hongyan Sun * Zhian Zhang, *

Mr. H. Li, Dr. J. Zhang, Dr. K. Cheng, Mr. Q. Chen, Dr. H. Sun

Department of Chemistry and COSDAF (Centre of Super-Diamond and Advanced Films), City University of Hong Kong, 83 Tat Chee Avenue, Kowloon, Hong Kong, China.

Mr. H. Li, L. He, X. Ge, Prof. Y. Lai, Prof. Z. Zhang

School of Metallurgy and Environment, Engineering Research Center of the Ministry of Education for Advanced Battery Materials, Hunan Provincial Key Laboratory of Nonferrous Value-Added Metallurgy Central South University, Changsha 410083, P. R. China

Mr. C. Guan

University of Michigan−Shanghai Jiao Tong University Joint Institute, Shanghai Jiao Tong University, Shanghai 200240, P. R. China

* Corresponding author email:

laiyanqing@csu.edu.cn

hongysun@cityu.edu.hk

zhangzhian@csu.edu.cn

Methods

Materials Synthesis

Synthesis of NMFPP: The NMFPP materials were synthesized by a solid-state method. A stoichiometric amount of $Na_4P_2O_7 \cdot 10H_2O$ (AR, Aladdin), $MnC_2O_4 \cdot 2H_2O$ (Mn 30%, Aladdin), $FeC_2O_4 \cdot 2H_2O$ (AR, Aladdin), and $NH_4H_2PO_4$ (AR, Aladdin) was fully mixed in a mortar. Then, the mixture was primarily calcined at 350 °C for 4h under Ar atmosphere. The resulting powder was ground and pelletized into plates and sintered again at 600 °C for 10 h under Ar atmosphere to obtain the target products.

Synthesis of $Na_3V_2(PO_4)_2F_3$: The material was synthesized according to previous literature with slight modifications.[1] Stoichiometric amounts of ammonium vanadate, citric acid, ammonium dihydrogen phosphate and ammonium fluoride were adequately dissolved in 50 ml distilled water and stirring at 80 ℃ to form a gel and then dried at 120 °C in an oven. After that, the precursor was preheated at 350 °C for 3 h and calcinated at 650 °C for 10 h under Ar to obtain the final material.

Preparation of SP/PAA binder: Sericin protein (MW ~30000) was dissolved in deionized water at 85 °C for 2h to form a SP solution. Meanwhile, polyacrylic acid (PAA) was dissolved in deionized water at room temperature to form a PAA solution. The SP/PAA was obtained by mixing certain amounts of the PAA solution and SP solution together with magnetic stirring at 85 °C for 2h. The amount ratio of SP and PAA was controlled to be 2:1. The PVDF binder solution was prepared by dissolving PVDF powders in N-methyl-2-pyrrolidone (NMP, Sigma-Aldrich, anhydrous, 99.5%). Solid concentration of all the solutions is 3wt%.

Preparation of electrodes: The active material NMFPP powders (80 wt%) and carbon

black (10 wt%) were thoroughly mixed with binders (10 wt%) to form black slurry. Then, the slurry was cast on an Al foil and dried in air at 60 °C for 6 h, and further dried in vacuum at 80 °C overnight. The mass loading of active material is 1.2 ~ 1.5 mg cm^{-2}.

Materials characterization

The X-ray diffraction (XRD) data were collected by a PANalytical Empyrean 2 with Cu K$_\alpha$ radiation. The data for Rietveld refinement was collected in the 2θ range from 5° to 60° at a slow scan rate of 2° min^{-1}. Field-emission scanning electron microscopy (FE-SEM, QUANTA 250) and Transmission electron microscopy (TEM, TF 20) were used to study morphology and lattice structure of the materials. Viscometer (NDJ-9S) was used to determine viscosity of the solutions under room temperature. Fourier-transform infrared spectroscopy (FTIR) were performed on Bruker Vertex 70. Chemical structure of SP and surface bonding structure of the electrode were studied by X-ray photoelectron spectroscopy (XPS, Thermo Scientific K-Alpha). The fitting process was conducted using Avantage software. The thermal stability of the SP/PAA binder was measured by thermogravimetric analysis (TGA, 5500) in N$_2$ atmosphere with a heating rate of 10 °C min^{-1}. The concentration of Mn in the electrolyte was determined by inductively coupled plasma optical emission spectroscopy (ICP-OES, PerkinElmer ICP 2100).

Electrochemical tests

To test electrochemical performance of the electrodes, CR2032 coin cells were fabricated in a glove box filled with pure Ar. 1 M NaClO$_4$ dissolved in propylene

carbonate (PC) solution with 5 vol% addition of fluoroethylene carbonate (FEC) was used as electrolyte. Galvanostatic charge-discharge measurements were conducted on a Land battery testing system (CT2001A) in a voltage range of 1.5 ~ 4.5 V vs. Na/Na$^+$. The current 1C = 120 mA g^{-1}. Electrochemical workstation (PARSTAT 2273) was employed for electrochemical impedance spectroscopy (EIS) measurements and cyclic voltammetry (CV) tests. For the galvanostatic intermittent titration technique (GITT) measurements, a constant charge/discharge current of 0.05 C was lasted for 15 min, followed by an interrupted time for 60 min. For the self-discharging tests, the electrode was firstly charged to 4.5 V and then open circuited to see the changes of the potential. For the manganese dissolution test, the NMFPP/SP/PAA electrode and NMFPP/PVDF electrode with the same amounts of active materials (250 mg) were added into 20 mL electrolyte, respectively, and standing for 30 days.

DFT calculations

The density functional theory (DFT) calculations were conducted to study the interactions between sodium and different peptide chains. For obtaining the suitable initial model, the peptide chains were fully relaxed in the box with the lattice parameters a = 20 Å, b = 16 Å and c = 20 Å. All DFT calculations were performed by using the Vienna ab initio simulation package within the projector-augmented-wave (PAW) approach.[2] The Perdew-Burke-Ernzerhof (PBE) functionals based on the generalized-gradient approximation (GGA) were adopted to calculate the total energies of all configurations with the sampled k-point grids of $1 \times 2 \times 1$, the corresponding energy cutoff and force tolerance are 450 eV and 0.02 eV Å^{-1},

respectively.[3] And the Grimme dispersion correction (D3) is taken into account so as to resolve the van der Waals interactions.[4]

For the calculations of sodium adsorption, the adsorption energy can be defined as:[5]

$$E_{ad} = (E_{adsorbent} + E_{substrate}) - E_{adsorbed\,state}$$

Where $E_{adsorbent}$, $E_{substrate}$ and $E_{adsorbed\,state}$ represent the energy of single sodium atom, the peptide and the state of sodium adsorption on the chain, respectively. In addition, for the calculation of energy barriers of Na diffusion, the CI-NEB (Climbing Image Nudged Elastic Band) method was used and five initial images between two local energy minima structures are first set by linear interpolation and then fully relaxed.[6]
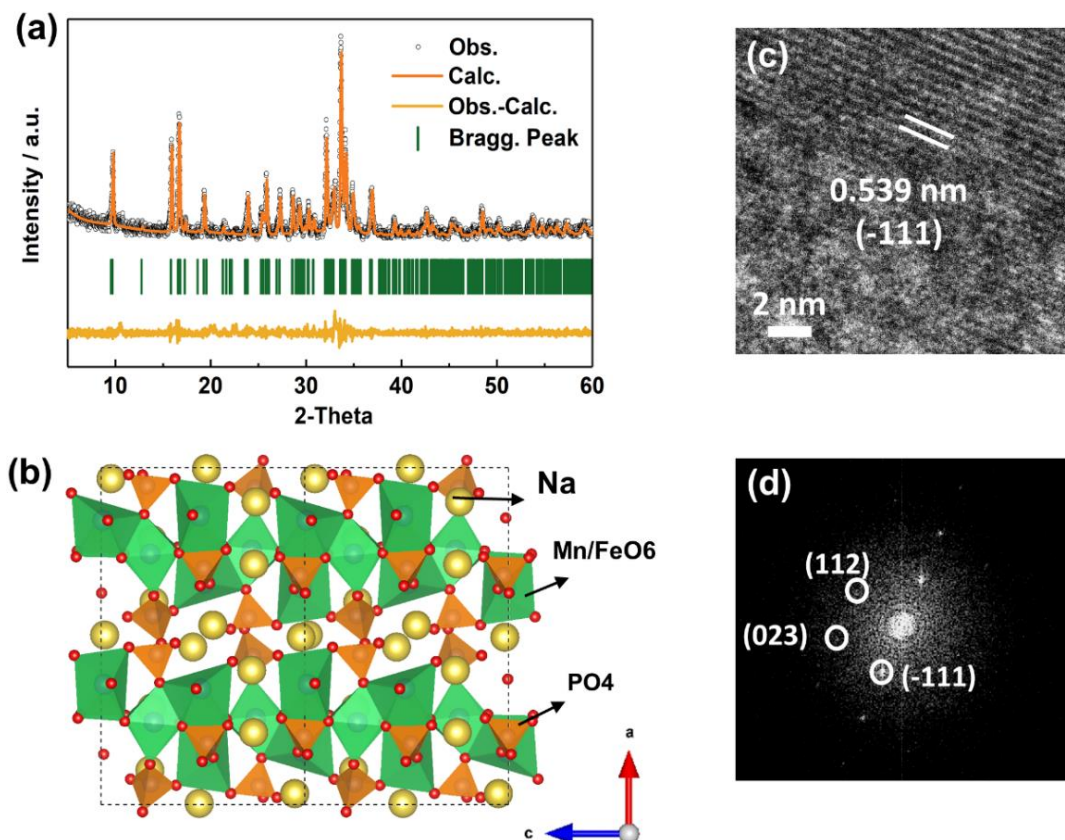
Figure S1. (a) Rietveld refinement profile of the NMFPP material. (b) Illustration of the crystal structure of NMFPP along the b-axis. (c) HRTEM image showing clear crystal lattice of NMFPP and (d) the orresponded fast Fourier transformation (FFT) pattern

The NMFPP adopts an orthorhombic structure with space group *Pn2₁a* (Figure S1a). In this structure, Mn/FeO6 octahedra and PO4 tetrahedra are connected by either co-edging or corner-sharing manners to form the [Mn2FeP2O13]∞ infinite layers that parallel to the bc plane. These infinite layers are then linked by P2O7 groups along the a-axis, leading to a 3D framework structure (Figure S1b). Details of the Rietveld refinement result and atomic potion of the materials are listed in Table S1. Diffraction

spots of the FFT pattern was identified as (112), (023) and (-111) facets of the
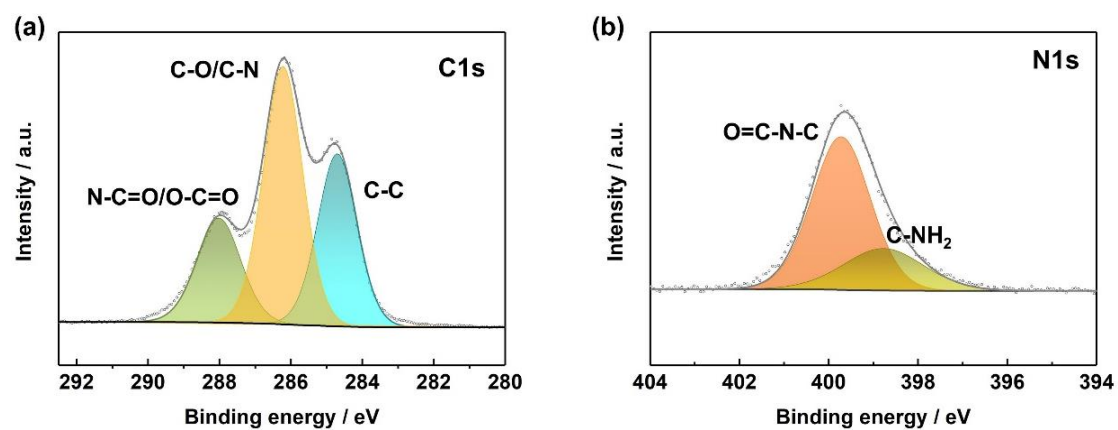
orthorhombic *Pn2$_1$a* phase (Figure S1d).

Figure S2. XPS characterization of sericin protein. (a) The high-resolution spectra of

C1s and (b) N1s.

Figure S3. Photographs of the binder films. The films were obtained by dropping the binder solutions in polytetrafluoroethylene (PTFE) moulds and dried in an oven at 60 °C under air.
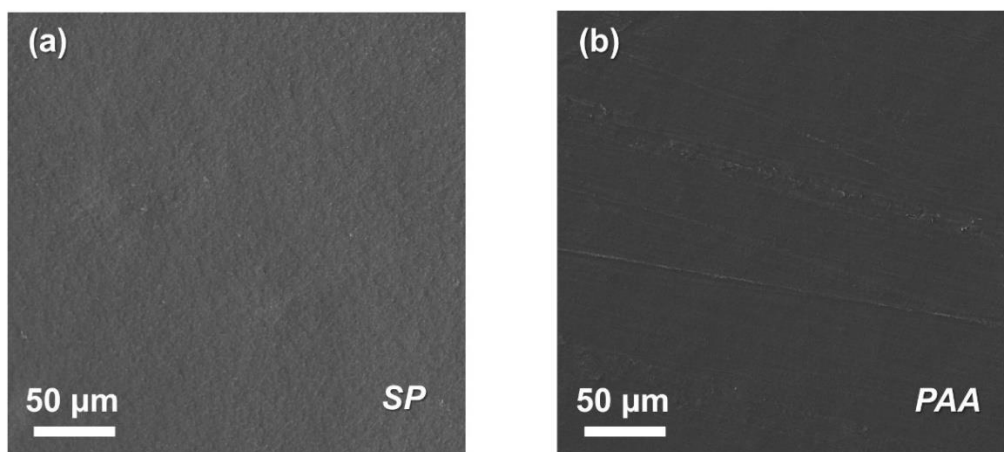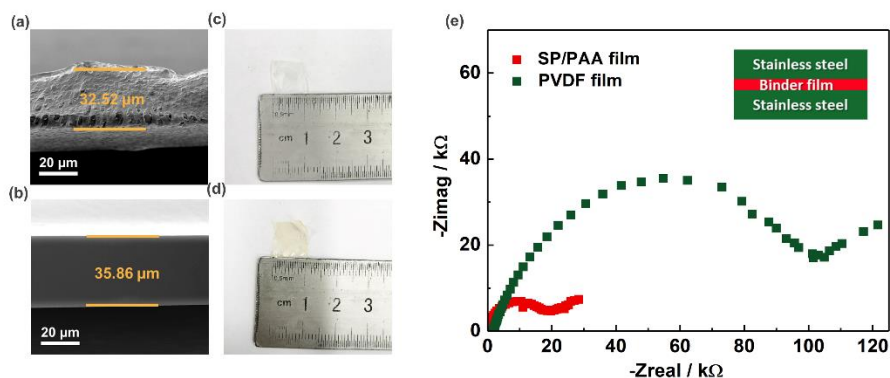
Figure S4. SEM images of the (a) SP film and (b) PAA film.

Figure S5. (a) SEM cross-section images of the PVDF film and (b) SP/PAA film. (c) Photograph of the PVDF film and (d) SP/PAA film. (e) EIS spectra of the films.

The binder films were firstly immersed in electrolyte for 1h and then taken from the electrolyte. The residual electrolyte was removed by tissue paper. The obtained films were then blocked by two stainless steels (inset) and sealed in a 2032-coin-cell for measurements. The EIS was conducted in a frequency range from 10000 Hz to 0.01 Hz with an amplitude of 10 mV. As shown in Figure S5, Nyquist spectra with one semicircle of is observed for each film, and the value of film resistance (R) can be calculated from the diameter of the semicircle.[7] The ionic conductivity can be obtained using the relationship

$$\sigma = D /(RS) \tag{1}$$

where σ represents ionic conductivity, D and S is the thickness and area of the film, respectively. Thickness of the PVDF and SP/PAA film is 32.52 μm and 35.86 μm, respectively. Areas of both films are 1 cm^2.
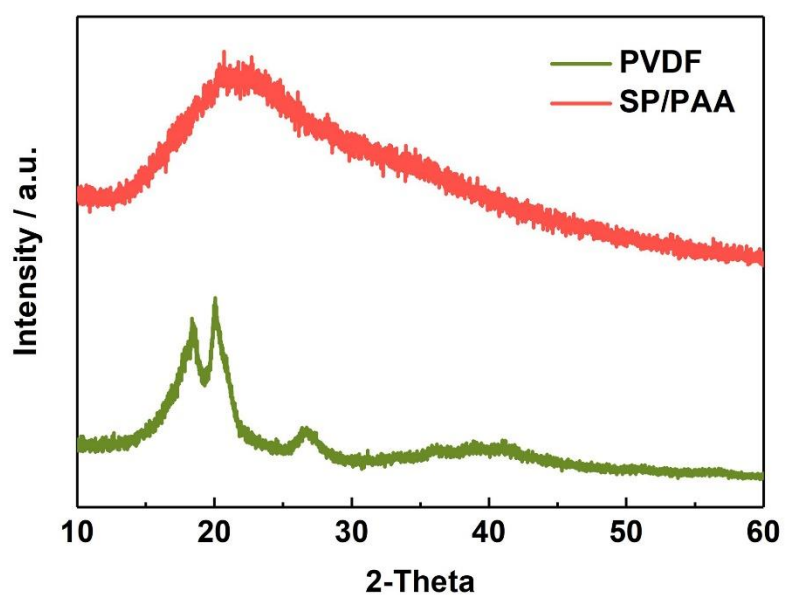
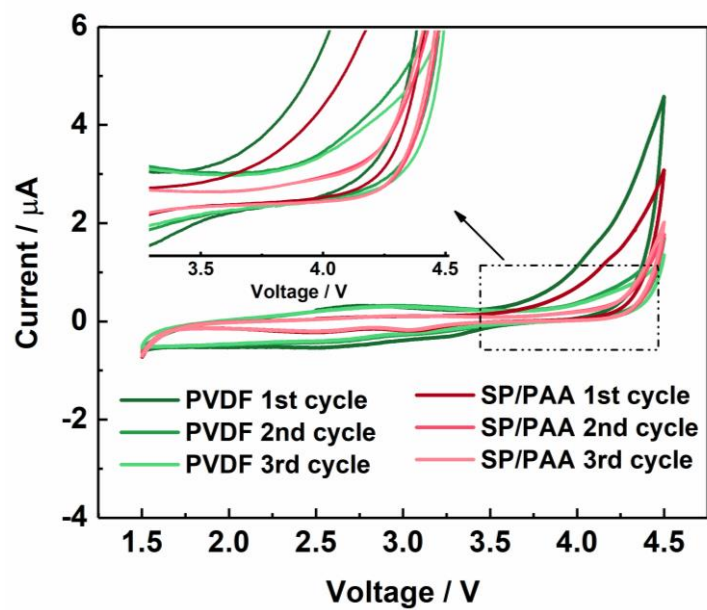**Figure S6.** XRD patterns of the PVDF and SP/PAA films.

Figure S7. CV curves for pure PVDF and SP/PAA films within the voltage window from 1.5 to 4.5 V at scan rate of 0.1 mV s^{-1}.
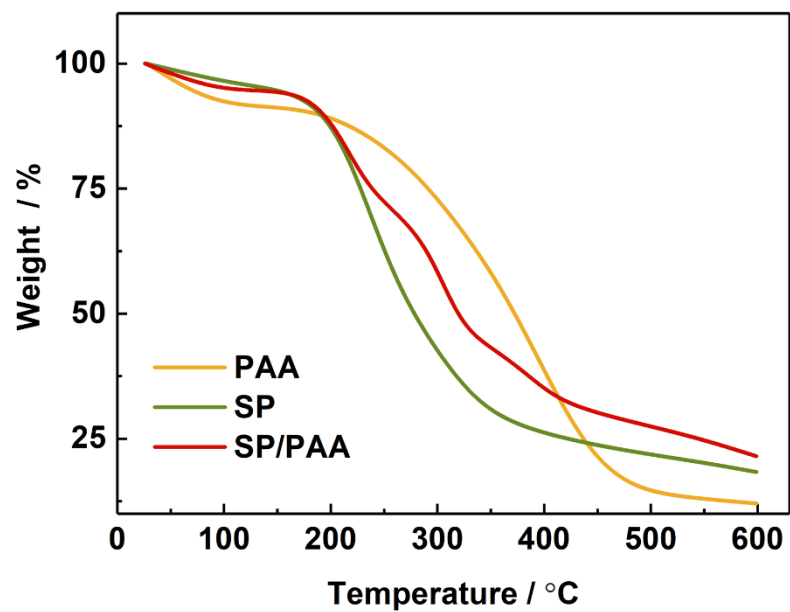
Figure S8. Thermal stability of SP/PAA binder measured by TGA in nitrogen gas from
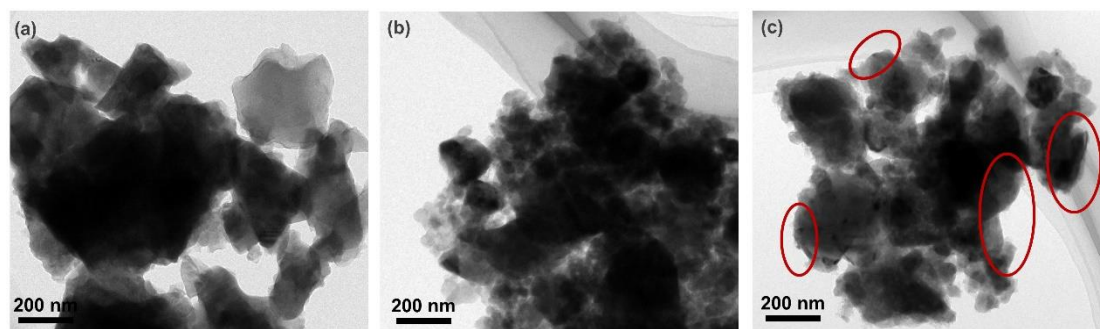
room temperature to 600 °C.

Figure S9. (a) TEM image showing the morphology of pure NMFPP particles. (b) TEM image showing the morphology of NMFPP electrode using SP/PAA binder and (c) PVDF binder. The red circles highlight the bare NMFPP surface.
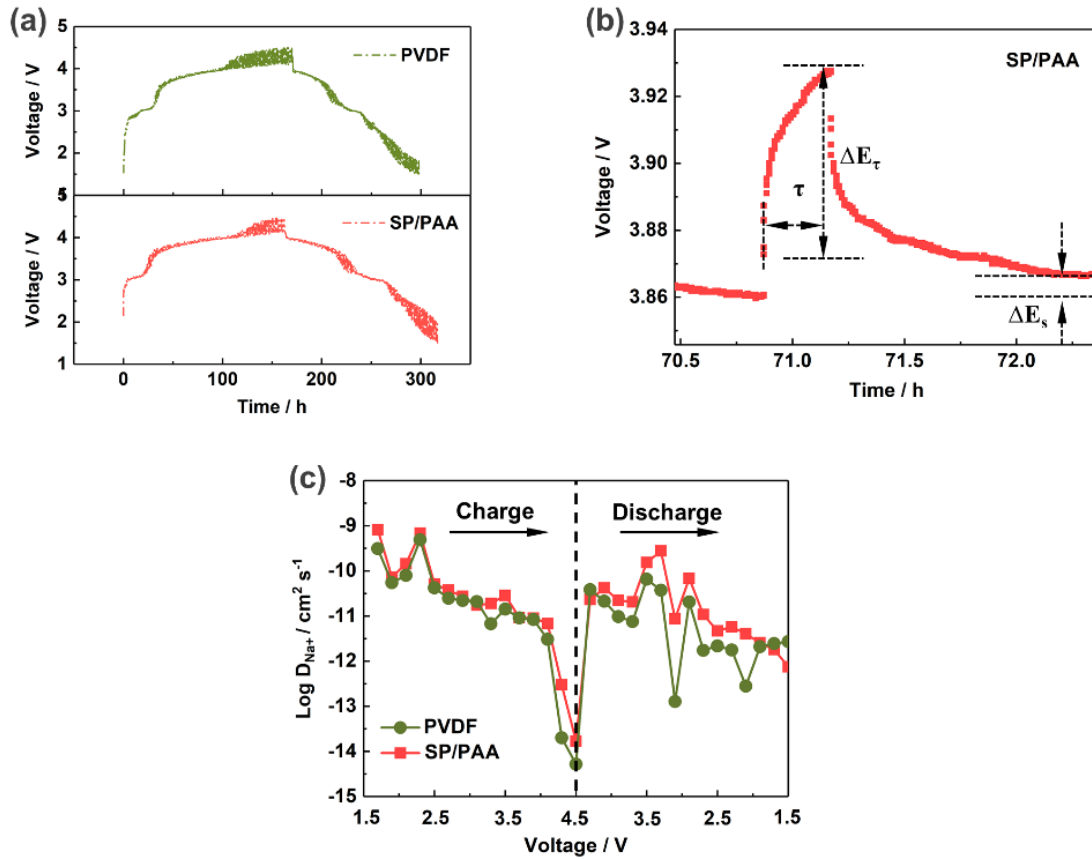
Figure S10. (a) GITT profiles of the electrodes. (b) Schematic diagram of a typical GITT titration step during charge process. (c) The variation of apparent sodium-ion diffusion coefficient (D_{Na+}) during sodium storage process.

Calculations of D_{Na} were based on the equation:[8]

$$D_{Na^+} = \frac{4}{\pi\tau}(\frac{m_B V_m}{M_B S})^2 (\frac{\Delta E_s}{\Delta E_\tau})^2 \qquad (\tau << \frac{l^2}{D_{Na^+}}) \tag{2}$$

Where m_B, M_B, V_m, S represent mass, molecular weight, molar volume and surface area of the electrode materials, respectively. ΔE_s is the difference between two consecutive stable voltages after relaxation, and ΔE_τ is the transient voltage-change during a single titration step.
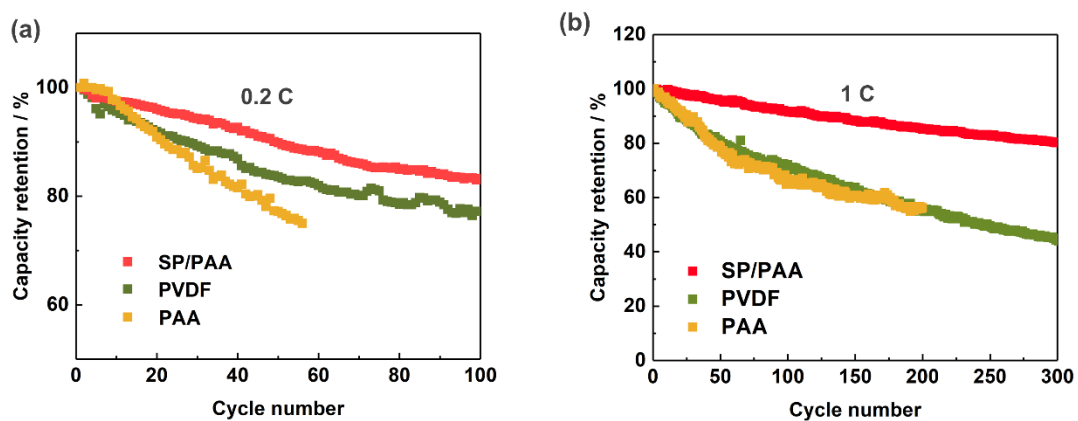
Figure S11. Capacity retention of the electrodes that cycling at (a) 0.2 C and (b) 1 C.
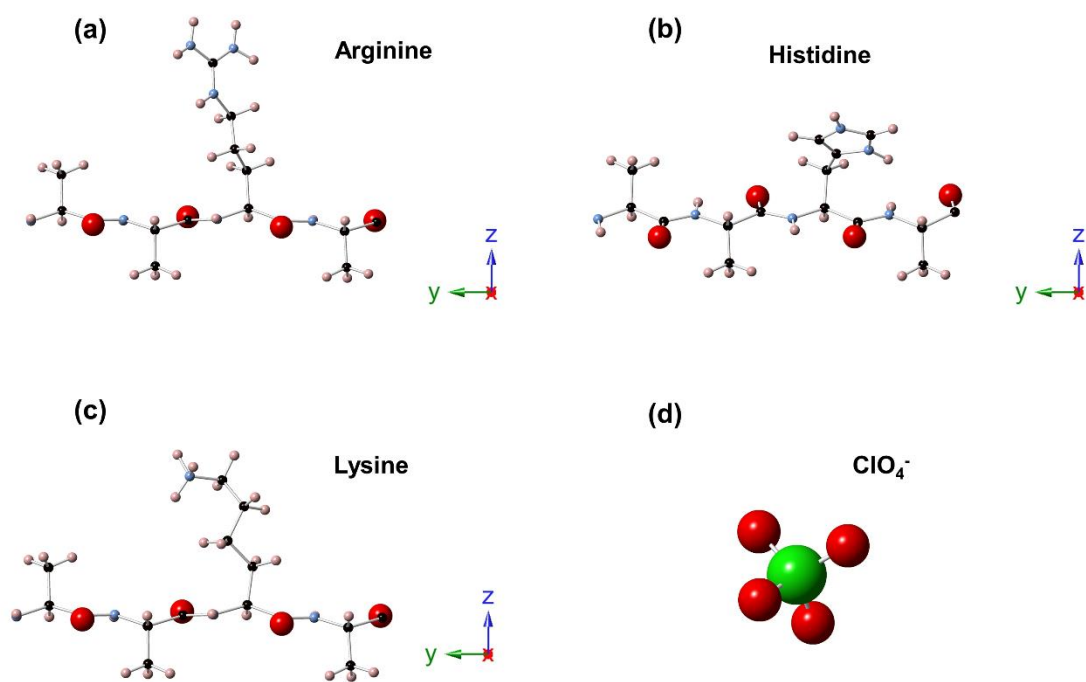
(a) Arginine

(b) Histidine

(c) Lysine

(d) ClO_4^-

Figure S12. Geometric structure of (a) arginine, (b) histidine, (c) lysine, and (d) ClO_4^- anion group.
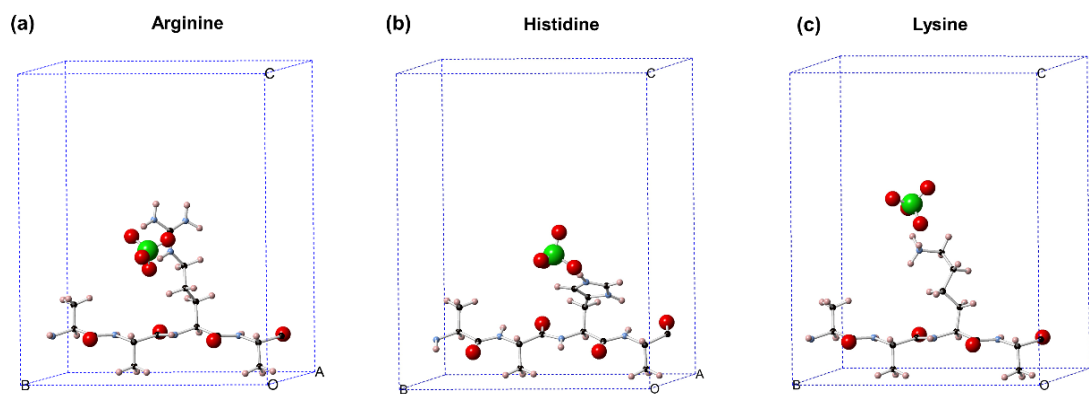
Figure S13. The stable modes showing the interaction between (a) arginine, (b) histidine, (c) lysine and the ClO_4^- anion group in the electrolyte.
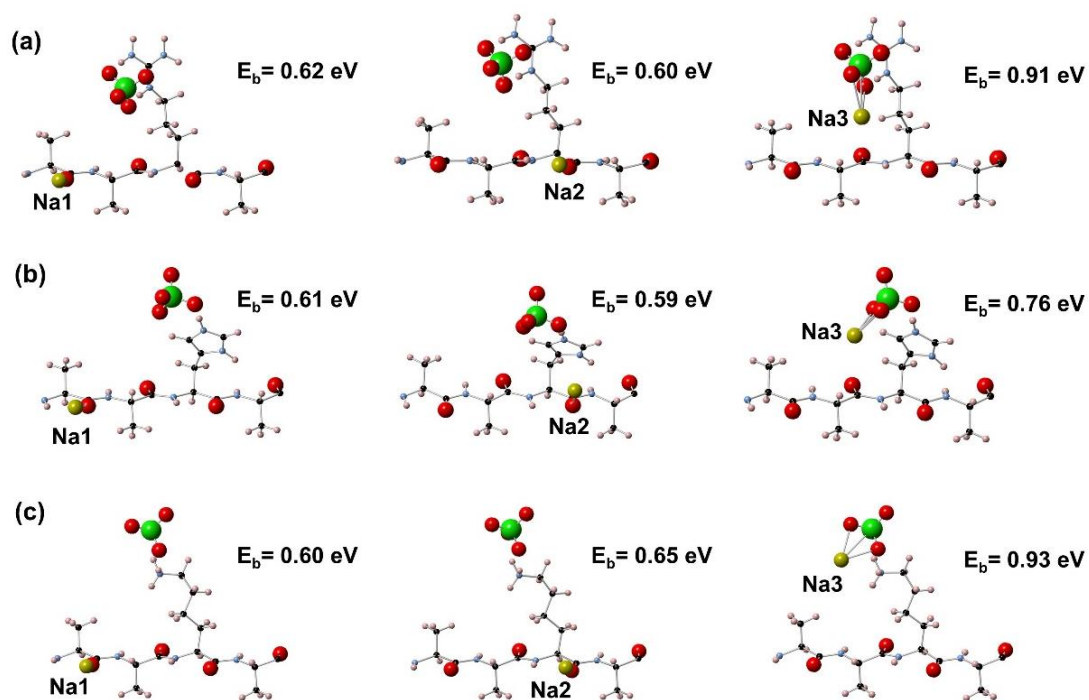
Figure S14. Configurations of the different Na^+ binding positions and the corresponding binding energies at (a) arginine, (b) histidine, (c) lysine.
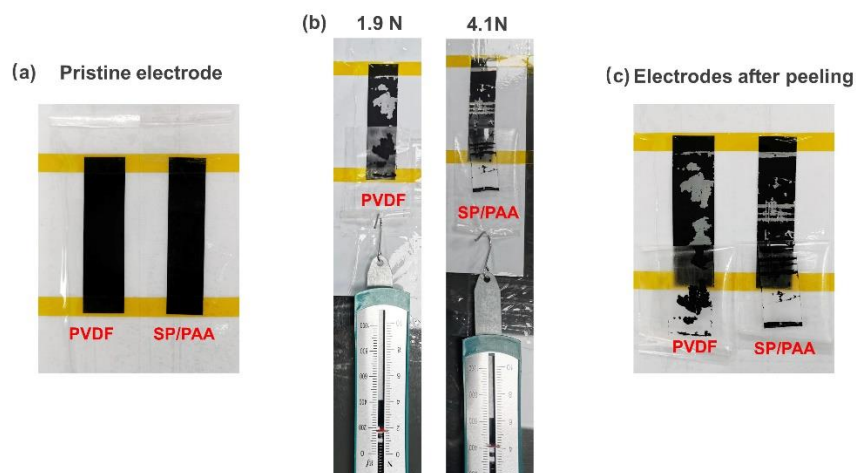
Figure S15. Stretch test of the adhesive force for PVDF and SP/PAA-based NMFPP electrodes. (a) Photograph of the pristine electrodes. (b) The adhesive force demonstrated during peeling process of the electrodes. (c) Photograph of the electrode after peeling.

(a)

(b)

(c)

(d)

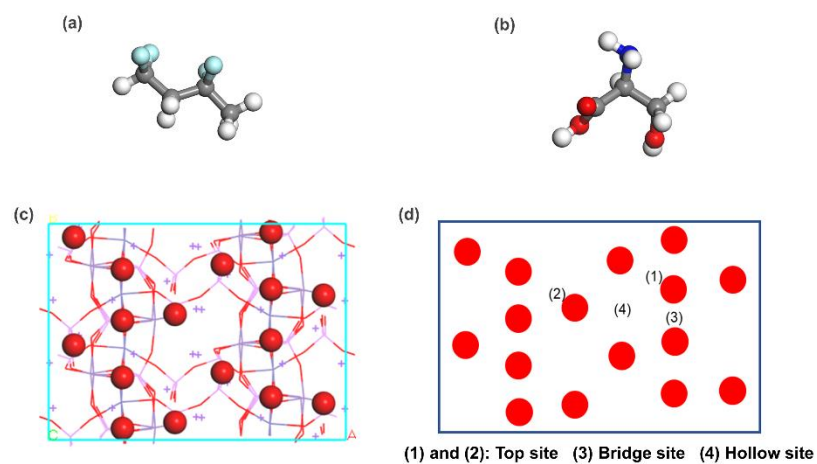(1) and (2): Top site   (3) Bridge site   (4) Hollow site

Figure S16. Geometric structure of (a) PVDF and (b) serine. (c) The arrangement of terminated oxygen atom of the NMFPP (001) surface. (d) Illustration of the four adsorption sites.
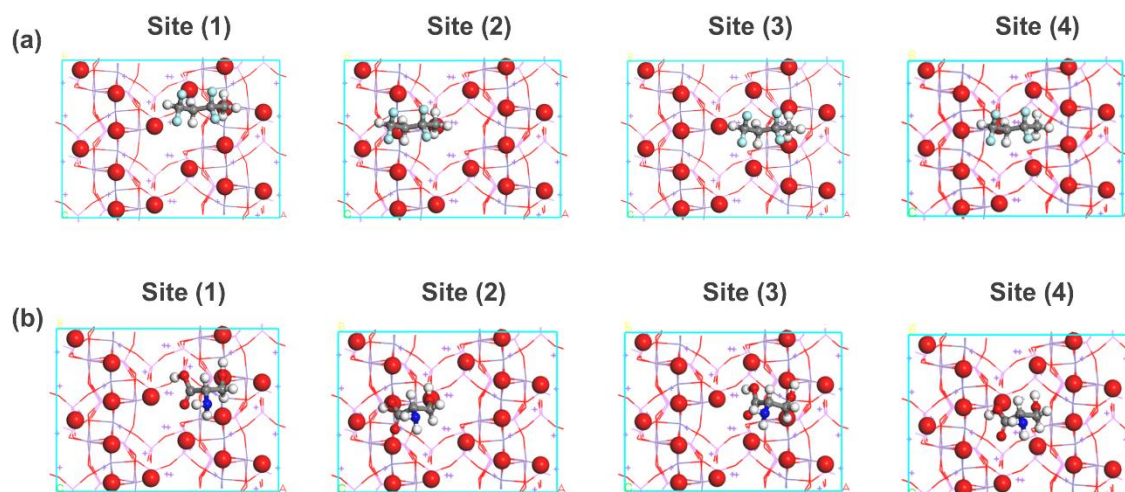
Figure S17. The configurations for (a) PVDF and (b) serine adsorption on the different sites of the NMFPP (001) surface.

According to the structural symmetry of NMFPP, four sites are chosen for the adsorption calculation of PVDF and serine. As shown in Figure S16, the arrangement terminated oxygen atom of the NMFPP (001) surface and the corresponding adsorption sites for PVDF and serine has been labelled. For the adsorption of PVDF and serine, the configurations are shown in Figure S17, the corresponding adsorption energies are listed in Table S2. Comparing the adsorption energy of different configurations, the adsorption energies of serine are more negative than that of PVDF on all sites, suggesting the stronger interaction between serine and NMFPP (001) surface. It also shows that the most stable adsorption site for PVDF is the site (4), and the most stable adsorption site for serine is the site (3) because these two sites show the lowest adsorption energies.
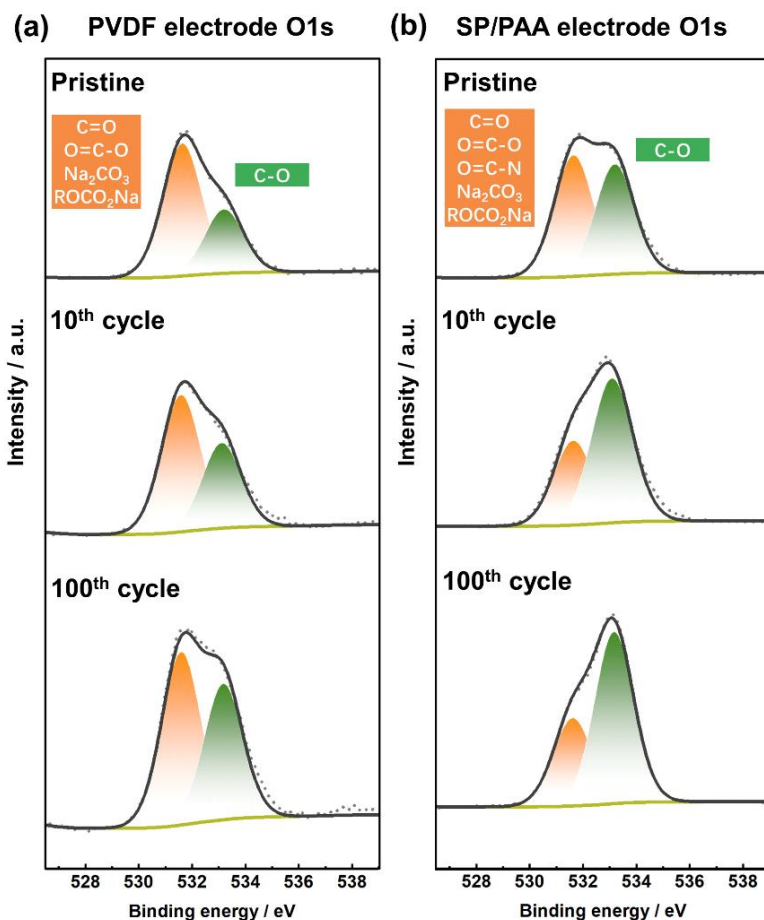
Figure S18. The surface composition evolution of the PVDF and SP/PAA-based electrodes upon cycling disclosed by high-resolution XPS. (a) O1s of PVDF and (b) O1s of SP/PAA-based NMFPP electrode.

The relative ratio of C-O peak (~533.3 eV) in the pristine PVDF electrode is smaller than that of the SP/PAA electrode, which is due to the initial presence of C-O group in sericin. During cycling, it can be seen that the ratio of cathode/electrolyte interphase composition (~531.7 eV) keeps increase for the PVDF electrode, while they keep constant after 10 cycles for the SP/PAA electrode. This phenomenon is in accord with the results of C1s.
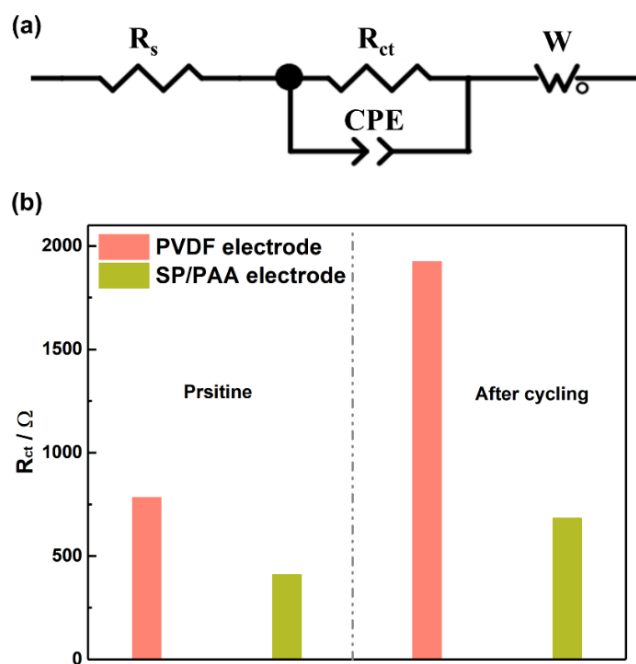
Figure S19. (a) The equivalent circuit models used to fit the EIS date. (b) Fitting results of the charge-transfer resistances (R_{ct}) of the electrodes before and after cycling.
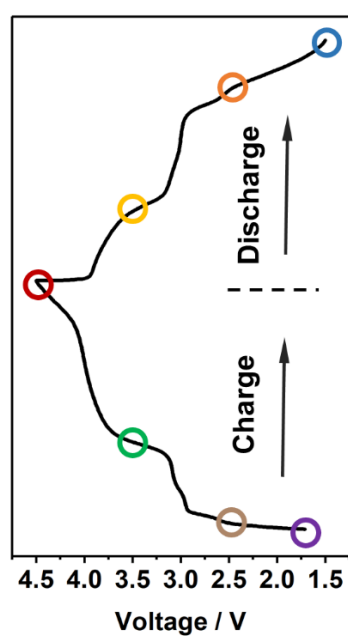
Figure S20. Charge/discharge profiles and the points selected for XRD characterization.
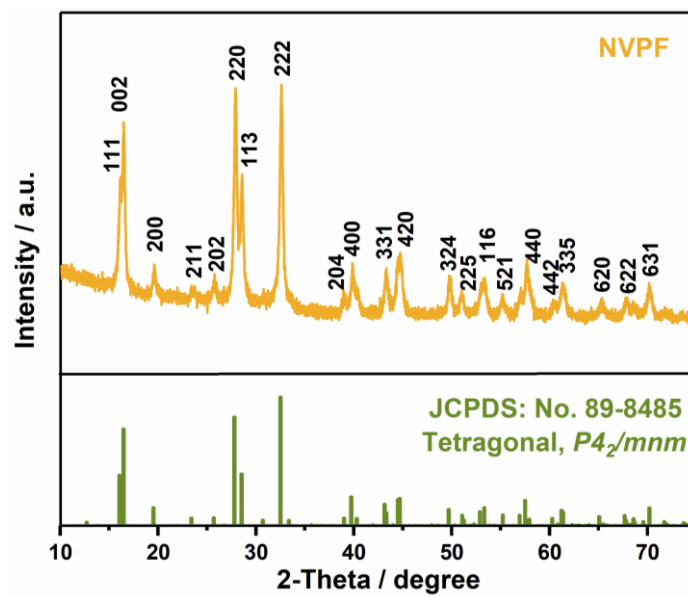
Figure S21. XRD of the as-synthesized NVPF cathode material.
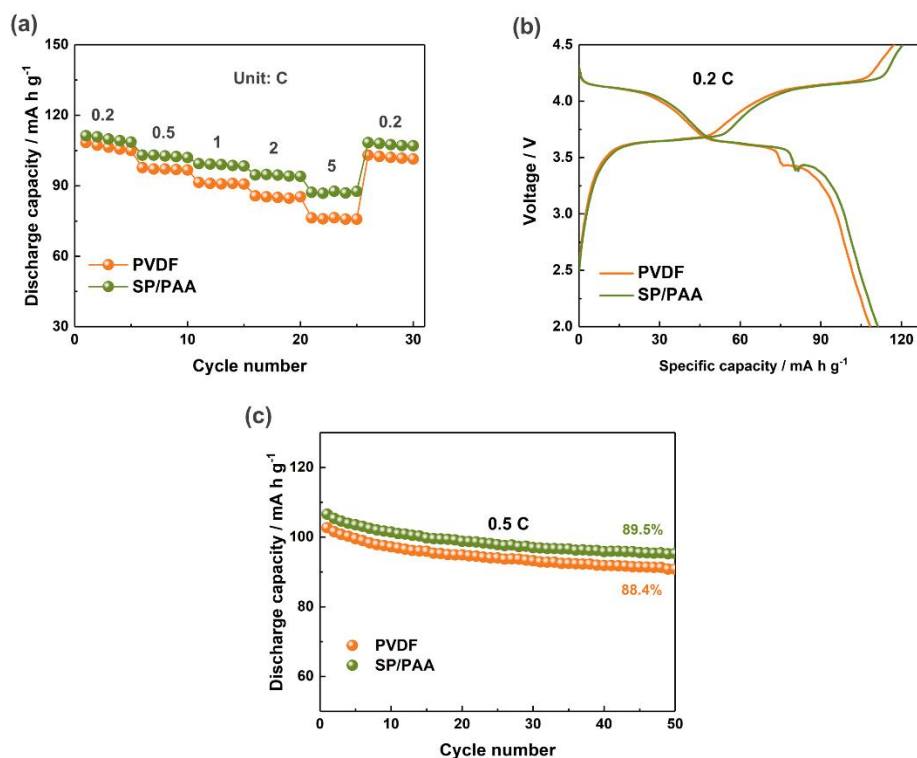
Figure S22. Electrochemical performance of NVPF electrodes made up from different binders. (a) Rate performance of the electrodes from 0.2 C to 5 C (1 C = 130 mA g^{-1}). (b) The charge/discharge profiles at 0.2 C. (c) Cycling performance at 0.5 C.

The SP/PAA-based NVPF cathode is able to deliver a discharge capacity of 111.3, 103.0, 99.4, 94.6, and 87.2 at 0.2, 0.5, 1, 2, and 5 C, respectively, which is higher than that of the PVDF-based NVPF cathode under the diverse C-rates (Figure S22a). In Figure S22b, a high working voltage platform centered at around 4.15 V can be observed. While such high voltage does not affect stability of the protein-based binder, as the electrode shows better cycling stability than that of the PVDF counterpart (Figure S22c).

Table S1. Detailed structural information of NMFPP derived from Rietveld refinement

space group = *Pna2₁*	Rp = 9.53 %	Rwp = 13.42 %
a (Å) = 18.0760	b (Å) = 6.5352	c (Å) = 10.6435
α (°) = 90	β (°) = 90	γ (°) = 90
V (Å³) = 1257.32		

Atom	x (Å)	y (Å)	z (Å)	frac	Uiso
Na1	0.49521 (12)	0.77569 (4)	0.98242 (11)	1	0.2736
Na2	0.28566 (7)	0.80615 (3)	0.73986 (20)	1	0.2736
Na3	0.41353 (8)	0.39022 (3)	0.26185 (18)	1	0.2736
Na4	0.47154 (10)	0.64898	0.54365 (14)	1	0.2736
Mn1	0.3691 (7)	0.07856 (4)	0.48829 (17)	0.5	0.16881
Mn2	0.14658 (7)	0.53568 (4)	0.48552 (17)	0.5	0.16881
Mn3	0.24215 (9)	0.28353 (3)	0.73965 (2)	0.5	0.16881
Fe1	0.3691 (7)	0.07856 (4)	0.48829 (17)	0.5	0.16881
Fe2	0.14658 (7)	0.53568 (4)	0.48552 (17)	0.5	0.16881
Fe3	0.24215 (9)	0.28353 (3)	0.73965 (2)	0.5	0.16881
P1	0.29179 (5)	0.54263 (3)	0.48459 (9)	1	0.08984
P2	0.17894 (5)	0.03118 (3)	0.49124 (10)	1	0.08984
P3	0.54587 (6)	0.41733 (3)	0.74681 (12)	1	0.08984
P4	0.44831 (5)	0.14161 (3)	0.7107 (11)	1	0.08984
O1	0.23601 (6)	0.46214 (3)	0.6223 (11)	1	0.08558
O2	0.36782 (7)	0.3941 (3)	0.5297 (11)	1	0.08558
O3	0.33091 (6)	0.81122 (3)	0.52325 (11)	1	0.08558
O4	0.26855 (6)	0.5657 (3)	0.40517 (10)	1	0.08558
O5	0.22755 (6)	-0.02767 (3)	0.40235 (10)	1	0.08558
O6	0.144 (6)	-0.12294 (3)	0.50497 (13)	1	0.08558
O7	0.28673 (6)	0.07615 (3)	0.60327 (12)	1	0.08558
O8	0.1402 (7)	0.22197 (3)	0.48119 (10)	1	0.08558
O9	0.4637 (6)	0.34012 (3)	0.70808 (9)	1	0.08558
O10	0.51127 (6)	0.50199 (3)	0.86873 (9)	1	0.08558
O11	0.61934 (5)	0.39262 (3)	0.71663 (12)	1	0.08558
O12	0.63311 (5)	0.61611 (3)	0.74362 (9)	1	0.08558
O13	0.41922 (6)	0.17631 (3)	0.86898 (11)	1	0.08558
O14	0.37418 (5)	0.35116 (3)	0.71311 (10)	1	0.08558
O15	0.52239 (6)	-0.07434 (3)	0.60533 (12)	1	0.08558

Table S2. The adsorption energies (eV) of PVDF and serine on different sites of NMFPP (001) surface.

	Site (1)	Site (2)	Site (3)	Site (4)
PVDF	-0.86	-0.81	-0.88	-0.98
Serine	-1.77	-1.62	-1.78	-1.69

References

[1]　T. Wang, W. Zhang, H. Li, J. Hu, Y. Lai, Z. Zhang, *ACS Appl. Energy Mater.* **2020**, *3*, 3845.

[2]　G. Sun, J. Kürti, P. Rajczy, M. Kertesz, J. Hafner, G. Kresse, *J. Molecular Structure: THEOCHEM* **2003**, *624*, 37.

[3]　J. P. Perdew, K. Burke, M. Ernzerhof, *Phy. Rev. Lett.* **1996**, *77*, 3865.

[4]　S. Grimme, J. Antony, S. Ehrlich, H. Krieg, *J. Chem. Phy.* **2010**, *132*, 154104.

[5]　S. Mukherjee, L. Kavalsky, C. V. Singh, *ACS Appl. Mater. Interfaces* **2018**, *10*, 8630.

[6]　B. Gao, R. Jalem, Y. Ma, Y. Tateyama, *Chem. Mater.* **2019**, *32*, 85.

[7]　X. Li, Y. Zhao, L. Cheng, M. Yan, X. Zheng, Z. Gao, Z. Jiang, *J. Solid State Electrochem.* **2005**, *9*, 609.

[8]　K. Tang, X. Yu, J. Sun, H. Li, X. Huang, *Electrochim. Acta* **2011**, *56*, 4869.